

Three-dimensional numerical analysis of convection and conduction cooling of spherical biocrystals with localized heating from synchrotron X-ray beams

Ashutosh Mhaisekar, Michael J. Kazmierczak* and Rupak Banerjee

Department of Mechanical, Industrial and Nuclear Engineering, University of Cincinnati, Cincinnati, OH 45221-0072, USA. E-mail: mike.kazmierczak@uc.edu

The differential momentum and thermal energy equations for fluid flow and convective heat-transfer around the sample biocrystal, with coupled internal heat conduction, are solved using advanced computational fluid dynamics techniques. Average \bar{h} as well as local h_θ values of the convective heat-transfer coefficients are obtained from the fundamental equations. The results of these numerical solutions show the three-dimensional fluid flow field around the sample in conjunction with the detailed internal temperature distribution inside the crystal. The external temperature rise and maximum internal temperature increase are reported for various cases. The effect of the important system parameters, such as gas velocity and properties, crystal size and thermal conductivity and incident beam conditions (intensity and beam size), are all illustrated with comparative examples. For the reference case, an external temperature rise of 7 K and internal temperature increase of 0.5 K are calculated for a 200 μm -diameter cryocooled spherical biocrystal subjected to a 13 keV X-ray beam of 4×10^{14} photons $\text{s}^{-1} \text{mm}^{-2}$ flux density striking half the sample. For all the cases investigated, numerical analysis shows that the controlling thermal resistance is the rate of convective heat-transfer and not internal conduction. Thermal diffusion results in efficient thermal spreading of the deposited energy and this results in almost uniform internal crystal temperatures ($\Delta T_{\text{internal}} \simeq 0.5$ K), in spite of the non-uniform h_θ with no more than 1.3 K internal temperature difference for the worst case of localized and focused beam heating. Rather, the major temperature variation occurs between the outer surface of the crystal/loop system and the gas stream, $T_s - T_{\text{gas}}$, which itself is only about $\Delta T_{\text{external}} \simeq 5\text{--}10$ K, and depends on the thermal loading imposed by the X-ray beam, the rate of convection and the size of the loop/crystal system.

1. Introduction

The problem of heat transfer from X-ray heated biocrystals has attracted crystallographers' attention in recent years. Subjecting the biocrystal to a third-generation synchrotron X-ray beam results in both thermal loading and radiation damage to the crystals. Cryogenic cooling of the biosample has been shown to help alleviate the radiation damage problem to a great extent and therefore has become standard practice (Hope, 1990; Rodgers, 1994; Garman & Schneider, 1997; Garman, 1999). Unfortunately, it has been shown (as reported in past radiation damage workshops and in the recent literature) that specific molecular 'structural' changes still occur to the macromolecules when exposed to third-generation

sources, even when held at cryogenic temperatures (Weik *et al.*, 2000). Hence, radiation damage is a very important area of ongoing research that involves many issues. Various different aspects of this complex problem are dealt with in great detail elsewhere, in other articles in this issue. The focus of this study is on the convection and conduction cooling of a cryocooled biocrystal sample from a pure thermal heat-transfer point of view. More specifically, the aim of this present analysis is to accurately determine the external and internal maximum temperature increase, and the heat-transfer rate from the biocrystal to the cooling cryostream.

Available thermal models, for predicting temperature rise owing to the absorption of X-ray beam energy, range in sophistication from simple to more advanced methodology.

The very basic ‘adiabatic’ analysis (Helliwell, 1992) is often used in predicting the maximum rate of temperature increase (K s^{-1}) of a crystal of a given mass having arbitrary shape. However, it does not consider the energy transport away from the biocrystal to the gas stream (*i.e.* the convection term is neglected). Such a model is reasonable only in the initial stage of the X-ray beam exposure and cannot be used to determine the actual final temperature of the crystal. Kuzay *et al.* (2001) and Kazmierczak (2001) included the convective heat-transfer coefficient in the model for the first time, although an estimated value, to predict the temperature of the crystal at steady state along with a more realistic temperature rise and rate of increase through the entire heating process. Their work considered the ‘lumped’ and ‘distributed’ thermal models for an infinite plane layer, cube and rectangular flat plate considering two different orientations. Simultaneously, Nicholson *et al.* (2001) performed a three-dimensional finite-element analysis on a macromolecular crystal subjected to a third-generation synchrotron X-ray source and obtained: (i) the internal steady-state temperature distribution; (ii) the outside temperature drop; and (iii) the transient temperature response immediately after the beam is turned on. The shape of the macromolecular crystal and the surrounding mother liquor was approximated as an ellipsoid. Two different gases, N_2 and He, with estimated heat-transfer coefficient values of 300 and $800 \text{ W m}^{-2} \text{ K}^{-1}$, respectively, were used in their analysis. The next advance in modeling heat transfer from macromolecular crystals was carried out by Rosenbaum & Kazmierczak (2002) and Kriminski *et al.* (2003). These studies featured a more precise analysis of the convective heat-transfer coefficient from the biocrystal surface to the cooling gas stream based on the physical (velocity) and thermo-physical (viscosity, density *etc.*) properties of the gas. Rosenbaum & Kazmierczak (2002) approximated the biocrystal/mother-liquor geometry as a flat disc and obtained a one-dimensional analytical steady-state solution for the temperature distribution in the system as a function of the radius of the disc in the area illuminated by the beam, and in the region beyond. The convective heat-transfer coefficient that they used was calculated from Whitaker’s (1972) correlation for a sphere. This correlation uses gas velocity and gas fluid properties as parameters and is based on extensive experimental data. Kriminski *et al.* (2003) theoretically determined the convective heat-transfer coefficient (and its dependence on various gas flow parameters) by applying the boundary layer theory for viscous flow. They approximated the crystal surface as a flat plate to determine the external temperature rise. To obtain the steady-state internal temperature distribution, the one-dimensional heat conduction equation for spheres was employed.

It should be noted that all the thermal models cited thus far assumed the convective heat-transfer coefficient to be constant over the entire surface of the biocrystal (ellipsoid, disc and sphere), which is not the case in reality owing to the complex gas flow field around the crystal loop geometry. The present analysis goes beyond previous work to accurately obtain [*via* computational fluid dynamics (CFD)] the spatial

Table 1

The values of the thermophysical properties (density, specific heat capacity, thermal conductivity and viscosity) of N_2 and He gases at 100 K and 30 K, respectively, used in the numerical computations.

Gas properties	N_2 at 100 K	He at 30 K
ρ (kg m^{-3})	3.5	1.6
c_p ($\text{J kg}^{-1} \text{K}^{-1}$)	1000.6	5200
k ($\text{W m}^{-1} \text{K}^{-1}$)	0.0098	0.036
μ ($\text{kg m}^{-1} \text{s}^{-1}$)	6.65×10^{-6}	4.64×10^{-6}

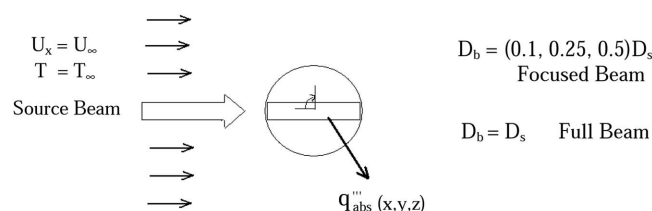


Figure 1

Schematic of the system of interest. The biocrystal, treated as a sphere, is exposed to an X-ray beam with absorption causing internal heating q''_{abs} . The source beam diameter is shown smaller than the sample size ($D_b < D_s$) but may be larger and irradiate the entire sphere ($D_b = D_s$). The sphere is immersed in a cooling gas stream with uniform upstream velocity U_∞ and constant temperature T_∞ .

variation of h_θ over the surface of the sphere, and thus allowing for the outer surface temperature to change accordingly while simultaneously calculating the temperature distribution within the biocrystal. A complete parametric study is also performed by varying the physical properties of the cryostream (velocity and gas type), and beam parameters (intensity and size), for various crystal sizes, to obtain the corresponding heat-transfer rate and the maximum internal and external temperature drops.

2. Mathematical formulation

The biocrystal and mother liquor geometry, approximated as a sphere, is subjected to an incoming X-ray beam and is convectively cooled in a stream of cold gas as shown in Fig. 1. Given this configuration, the sphere is internally heated owing to energy deposition and is externally cooled by convection with the cold gas stream. Two different gases, N_2 or He at different temperatures, 100 K and 30 K, respectively, are used to cool the sample. The thermophysical properties of N_2 and He gases are given in Table 1 at their respective temperatures. The target diameter of the incoming X-ray beam, D_b , can be reduced (focused beams) to either 10, 25 or 50% of the projected diameter of the sphere, D_s , or can be made the same size as the projected diameter of the sphere (full beam). The cold gas stream is treated as incompressible viscous flow and the upstream flow is assumed steady and unidirectional (*i.e.* constant uniform inlet velocity profile with single velocity component). The cooling gas stream (from jet nozzle outlet) is at a constant temperature T_∞ and a velocity of U_∞ . The three-dimensional domain and finite volume mesh, as shown in Fig. 2, was selected for the flow and conjugate heat-transfer

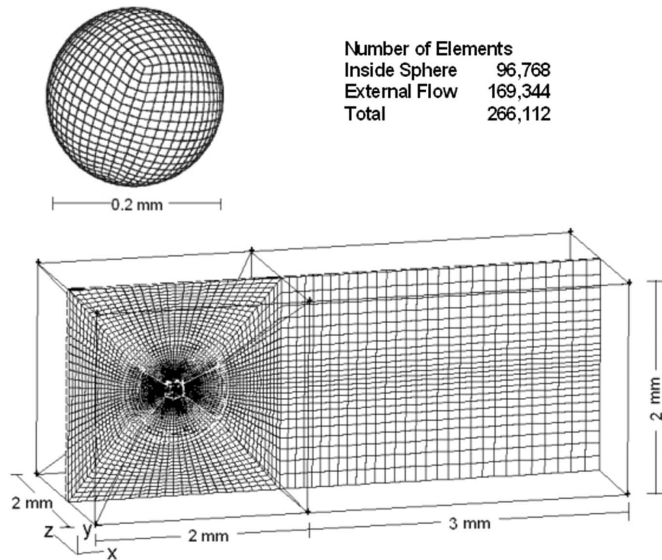


Figure 2 Computational domain used in the CFD analysis showing the finite volume mesh. The flow domain extends 20 sphere diameters downstream from the solid sphere in the axial flow direction and ten diameters in the direction normal to the flow direction (xy plane). Finer grid spacing is used in and near the sphere surface and in the wake region for greater accuracy.

analysis within and around the sphere. Though much research for flow over spheres in the past has dealt with a two-dimensional axisymmetric domain which uses the vorticity and stream function formulation approach, this study is based on the primitive variables formulation using velocity, pressure and temperature as primary degrees of freedom. The continuity and momentum equations for the flow field around the sphere are as follows,

$$\nabla \cdot (\rho \mathbf{v}) = 0, \quad (1)$$

$$\nabla \cdot (\rho \mathbf{v} \mathbf{v}) = -\nabla p + \nabla \cdot (\bar{\tau}) + \rho \cdot \mathbf{g}, \quad (2)$$

where ρ is the density, \mathbf{v} is the velocity vector, p is the static pressure, $\bar{\tau}$ is the stress tensor and $\rho \cdot \mathbf{g}$ is the gravitational body force. The stress tensor $\bar{\tau}$ is described as

$$\bar{\tau} = \mu(\nabla \cdot \mathbf{v} + \nabla \cdot \mathbf{v}^T), \quad (3)$$

where μ is the molecular viscosity. The differential thermal energy equation that gives the temperature field around the sphere is of the form

$$\rho c_p (\mathbf{v} \cdot \nabla T) = k_f \nabla^2 T, \quad (4)$$

where k_f is the thermal conductivity of the fluid, c_p is the heat capacity and ρ is the density of the fluid. The heat conduction equation in the solid region (sphere) is given by

$$k_s \nabla^2 T - S_h(x, y, z) = 0, \quad (5)$$

where k_s is the thermal conductivity of the solid, T is the temperature and S_h is the volumetric internal heat source (discussed separately in the following subsection). Specific boundary conditions are required to complete the formulation.

Flow boundary conditions are as follows:

(i) no slip boundary condition is considered on the wall of the sphere;

(ii) $U_x = U_\infty$, $U_y = 0$ and $U_z = 0$ at the inlet of the domain (uniform flow);

(iii) $U_x = U_\infty$, $U_y = 0$ and $U_z = 0$ on all the lateral surfaces of the external flow domain;

(iv) stress free at the outflow of the domain with gauge pressure being zero.

Thermal boundary conditions:

(i) $T = T_\infty$, constant temperature at inlet of the fluid flow domain;

(ii) $T = T_\infty$ on the lateral surface of the flow domain;

(iii) at outlet the temperature gradients in the direction of the flow are set to zero;

(iv) continuity of temperature and heat flux on the surface of the sphere.

The finite volume mesh was developed with hexahedral elements. The mesh was graded with a finer spacing in and around the wake region of the sphere so as to accurately model the flow and temperature fields. The solid sphere was represented by a total number of ~ 97000 hexahedral elements whereas ~ 170000 hexahedral elements were used in the flow domain surrounding the sphere. The domain size was chosen such that the length was 25 times and the width and height were 10 times the diameter of the sphere. Typical computational run time on a Pentium 4, 2.4 GHz with 1024 MB RAM, was about 3 h. More information regarding code validation and other numerical details can be found by Mhaisekar *et al.* (2005).

2.1. Heat source distribution

The internal heat source distribution within the sphere (Fig. 3) depends on the local absorption of the source beam, which, in turn, depends on the intensity of the source beam, depth of target and material characteristics (crystal composition). Mathematically the source term S_h depends strongly on spatial location and is given by

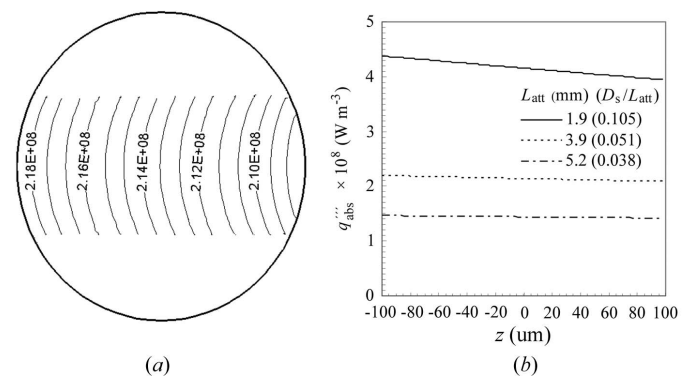


Figure 3 Internal heat source distribution inside the sphere when exposed to an X-ray beam of flux 3.14×10^{12} photons s^{-1} irradiating 50% of the sphere. (a) q''_{abs} contours (in $W m^{-3}$) plotted on the axial yz plane passing through the sphere center for $L_{att} = 3.9$ mm. (b) Axial profiles for all three different values of L_{att} studied.

Table 2
Summary of runs.

Case 1 serves as the reference case with results highlighted in italic in all subsequent tables. Parameters are varied as shown in runs 2–16 to illustrate their effect on the resulting heat transfer and crystal temperatures.

Case number	Gas velocity (m s ⁻¹)	k (W m ⁻¹ K ⁻¹)	Intensity (photons s ⁻¹ mm ⁻²)	L_{att} (mm)	Beam diameter (mm)	Crystal diameter (mm)	Gas type
1	<i>1</i>	<i>0.6</i>	4×10^{14}	3.9	<i>0.1</i>	<i>0.2</i>	N ₂
2	<i>0.5</i>	0.6	4×10^{14}	3.9	0.1	0.2	N ₂
3	<i>1.5</i>	0.6	4×10^{14}	3.9	0.1	0.2	N ₂
4	2	0.6	4×10^{14}	3.9	0.1	0.2	N ₂
5	1	<i>6</i>	4×10^{14}	3.9	0.1	0.2	N ₂
6	1	<i>0.06</i>	4×10^{14}	3.9	0.1	0.2	N ₂
7	1	0.6	4×10^{13}	3.9	0.1	0.2	N ₂
8	1	0.6	4×10^{15}	3.9	0.1	0.2	N ₂
9	1	0.6	4×10^{14}	<i>1.9</i>	0.1	0.2	N ₂
10	1	0.6	4×10^{14}	5.2	0.1	0.2	N ₂
11	1	0.6	1×10^{16}	3.9	<i>0.02</i>	0.2	N ₂
12	1	0.6	1.6×10^{15}	3.9	<i>0.05</i>	0.2	N ₂
13	1	0.6	1×10^{14}	3.9	<i>0.2</i>	0.2	N ₂
14	1	0.6	4×10^{14}	3.9	0.1	<i>0.4</i>	N ₂
15	1	0.6	4×10^{14}	3.9	0.1	<i>0.8</i>	N ₂
16	1	0.6	4×10^{14}	3.9	0.1	0.2	<i>He</i>

$$S_{\text{h}}(x, y, z) = q_{\text{gen}}''' = (I_o''/L_{\text{att}}) \exp(-L/L_{\text{att}}) \\ = (I_o''/L_{\text{att}}) \exp\left\{z - [(D_s/2)^2 - (x^2 + y^2)]^{1/2}/L_{\text{att}}\right\}, \quad (6)$$

where I_o'' is the incident intensity of the source beam, L is the depth of target (distance traveled through the sphere), L_{att} is the beam's attenuation length (material property that depends on the energy of the beam) and D_s is the diameter of the sphere. Fig. 3 shows the variation in energy deposition along a plane passing through the center of the biocrystal for the 'base' case. The beam source used here was a focused beam with a flux density of 4.0×10^{14} photons s⁻¹ mm⁻² and $L_{\text{att}} = 3.9$ mm (reference case) striking half of the biocrystal, *i.e.* $D_b = D_s/2$, and therefore 3.14×10^{12} photons s⁻¹ total flux into a 0.2 mm-diameter sphere. The source profiles for two other values of L_{att} , representing high and low values, are also plotted (to be considered later to determine its impact on temperature distribution). Besides absorption length, another important consideration in the source term is the size (*i.e.* target area) of the source beam. For the full beam, the source beam diameter is equal to the diameter of the sphere (0.2 mm for the base case) whereas for the focused beams the diameter of the source beam is reduced to half, one-quarter and one-tenth of the diameter of the sphere, and thus the flux densities are four, 16 and 100 times greater, respectively. However, it should be noted that the total incident power striking the sphere (flux into sample) is kept constant ($I_o''A_B = 3.14 \times 10^{12}$ photons s⁻¹) for all cases. This is achieved by increasing the incident intensity in the focused beam according to the following relation,

$$I_{0\text{Full}}''A_{\text{Full}} - I_{0\text{Fc}}''A_{\text{Fc}} = 3.14 \times 10^{12} \text{ photons s}^{-1}, \quad (7)$$

where A_{Fc} , A_{Full} and $I_{0\text{Fc}}''$, $I_{0\text{Full}}''$ are the areas and incident intensities of the focused and full beams, respectively. For the

focused beam, the power is absorbed in a cylindrical region passing through the sphere center.

3. Results and discussion

The sample consisting of crystal and mother liquor, approximated as a sphere, subjected to a third-generation X-ray beam is analyzed using the above-mentioned three-dimensional numerical finite volume model. The salient objectives of the present analysis are to accurately obtain the flow field around the biosample for a given gas velocity, surrounding temperature field, internal temperature distribution within the biosample and rate of convective heat transfer from the biocrystal to the cold stream. In all, 16 different cases were studied (see Table 2). The internal and external values of ΔT for various cases

are compared and the change in convective heat-transfer coefficient is studied by varying the gas velocity (runs 1–4), thermal conductivity of the crystal (runs 5–6), changing the intensity of the source beam (runs 7–8), altering the absorption length (runs 9–10), focusing the beam to smaller and larger size (runs 11–13), increasing the crystal size (for a constant beam size, runs 14–15) and, finally, changing the gas type (run 16). The results for the baseline case (run #1, in Table 2) give the complete details of the flow and heat transfer in and around the biocrystal for the given set of parameters. They are discussed first in depth and serve as the reference case for all the other runs investigated.

4. Baseline case results

The spherical biosample in the loop size of $D_s = 200$ μm is convectively cooled by the N₂ gas stream flowing over the sample at 100 K with a velocity of $U_{\text{gas}} = 1$ m s⁻¹. The source beam is a focused X-ray beam of size $D_b = 0.1$ mm (50% of D_{sphere}), with an intensity of 4×10^{14} photons s⁻¹ mm⁻² at 13 keV. For $L_{\text{att}} = 3.9$ mm the amount of energy absorbed in the biocrystal is equal to $q_{\text{abs}} = 0.308$ mW. The thermal conductivity of the biocrystal, k_{sphere} , is taken to be 0.6 W m⁻¹ K⁻¹. The parameters of the thermophysical properties of N₂ gas at 100 K, used in the computations, are shown in Table 1.

The flow field around the biocrystal, as depicted by the velocity vectors at mid-depth as viewed from the normal to the flow direction (YZ plane) at steady state, is shown in Fig. 4(a). The velocity vectors are color-coded with maximum velocity shown in red and minimum velocity in blue. There exists a complex flow field around the sphere and there are large variations in velocity in the immediate vicinity of the sphere's surface. A recirculation region is evident behind the sphere with the formation of a single axisymmetric donut-shaped

radiation damage

vortex owing to the combination of viscous shear forces and adverse pressure gradient caused by the spherical shape. The length of this region is dependent on the upstream flow velocity, or non-dimensional Reynolds number defined as $Re = \rho VL/\mu$ where ρ , V and μ are the density, velocity and viscosity of the fluid, respectively, and L is the characteristic length of the body, being the diameter D_{sphere} in this case.

Fig. 4(b) shows the temperature variation in the flowing gas stream surrounding the spherical biocrystal. The energy that is absorbed by the biosample owing to exposure to the X-ray beam must first be conducted to the outer wall, and is then carried away by the gas stream, as indicated by the temperature variation in the gas stream. The temperature gradients near the sphere surface are very large, especially in the very slender region near the front half of the sphere that forms the so-called thermal boundary layer. The temperature at the outer wall of the sphere is also shown and the rise in average wall temperature, \bar{T}_{wall} , above the free stream N_2 gas temperature owing to energy absorption is about 7 K.

The local heat-transfer coefficient, h_θ , varies spatially over the surface of the sphere because of the complex flow pattern. Fig. 5 shows h_θ plotted against the angular displacement along the surface of the biocrystal. The local heat transfer h_θ varies from a maximum value of $614 \text{ W m}^{-2} \text{ K}^{-1}$ at the stagnation

point at the front of the sphere to $130 \text{ W m}^{-2} \text{ K}^{-1}$ at the point of flow separation ($\theta \simeq 140^\circ$) before increasing slightly again at the rear of the crystal. This is due to the flow field near the sphere surface, which results in a maximum of the normal velocity gradient near the stagnation point. Gradually the velocity and its gradient reduce to zero at the point of flow separation. Away from the flow separation point the velocity increases again owing to the flow recirculation in the wake. The average convection heat-transfer coefficient is calculated by integrating the local value over the entire surface of the spherical crystal and is found to be $\bar{h} = 346 \text{ W m}^{-2} \text{ K}^{-1}$.

The temperature contours inside the sample at mid-depth from the side (YZ plane) and front (XY plane) are shown in Figs. 6(a) and 6(b), respectively. The energy is almost uniformly absorbed inside the central cylindrical core region of the biocrystal owing to the relatively large value of the absorption length of the source beam. The final steady temperature distribution shown is the result of the energy balance between the diffusion of the deposited energy (heat conduction) inside the solid and that convected from the outer surface. Fig. 6(a) indicates higher temperature in the rear of the biocrystal which is due to the lower local convective heat-transfer rate, h_θ , as shown in Fig. 5. The maximum internal

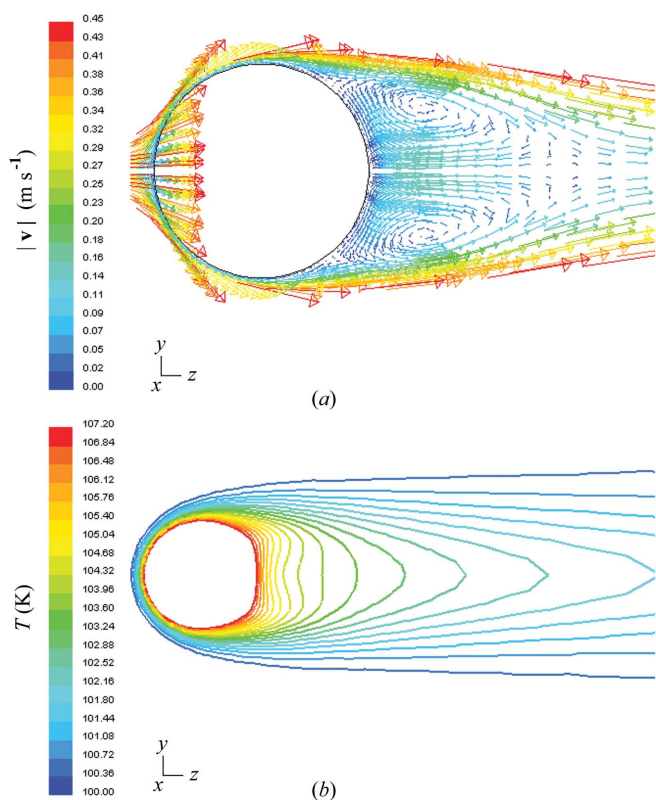


Figure 4 Numerical computations for the reference case: (a) the flow field past the sphere depicted by velocity vectors; (b) the temperature field in the gas stream surrounding the sphere as illustrated by isotherms. $\bar{T}_{\text{wall}} - T_\infty = 7.2 \text{ K}$. The velocity field shows the flow separation and the large recirculation region downstream of the sphere. Note that the thermal field and temperature gradients immediately before and after the sphere are considerably different owing to the presence of this large wake.

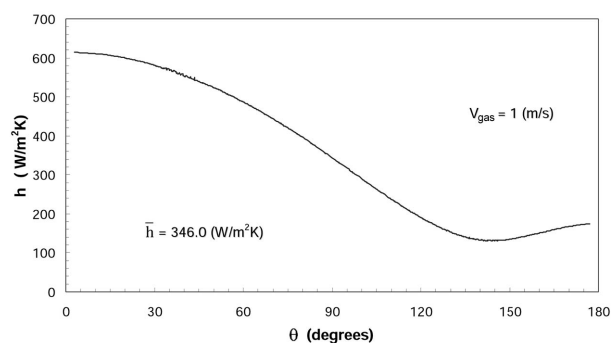


Figure 5 Variation of local h_θ along the surface of the sphere as calculated for the reference case. The temperature field results in a maximum h_θ value at the front stagnation point, $\theta = 0$, and a minimum value occurs at the point of flow separation, $\theta \simeq 140^\circ$.

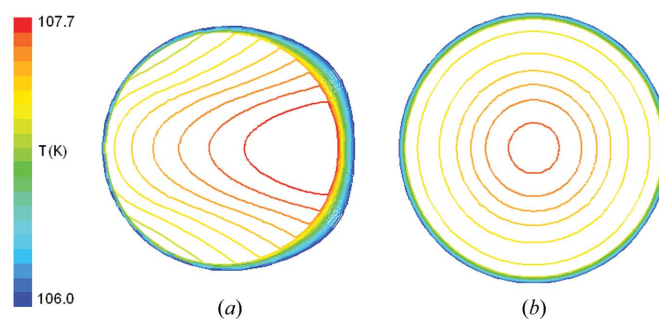


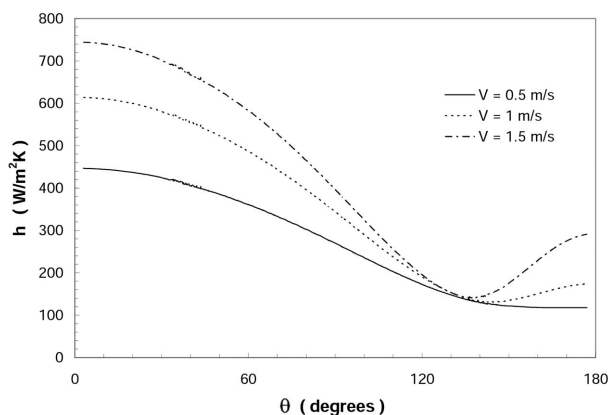
Figure 6 Temperature contours (isotherms) inside the sphere for the reference case plotted at mid-depth: (a) side view (YZ plane) and (b) front view (XY plane). $T_{\text{max}} - \bar{T}_{\text{wall}} = 0.56 \text{ K}$. The higher temperature in the rear of the sphere is due to lower local h_θ in the wake region. However, note that the temperature field inside the sphere plotted on the XY plane is axisymmetric (circumferentially symmetric in the direction normal to the flow stream although asymmetrical in the longitudinal flow direction).

Table 3

The effect of gas velocity on \bar{h} , $\Delta T_{\text{outside}}$ and $\Delta T_{\text{internal}}$ with all other parameters held at the reference case values.

With increasing velocity, \bar{h} increases and therefore reduces $\Delta T_{\text{outside}}$. However, $\Delta T_{\text{internal}}$ remains practically constant and independent of gas velocity.

Velocity (m s ⁻¹)	\bar{h} (W m ⁻² K ⁻¹)	$\bar{T}_{\text{wall}} - T_{\infty}$ (K)	$T_{\text{max}} - \bar{T}_{\text{wall}}$ (K)
0.5	269.3	9.22	0.537
1	346.0	7.16	0.556
1.5	406.7	6.06	0.543
2	458.3	5.88	0.560

**Figure 7**

The local heat-transfer coefficient h_{θ} versus θ calculated for various gas stream velocities. Comparison shows that the local value of h_{θ} increases as gas velocity increases at all locations except at the flow separation point.

temperature difference in the biosample, $\Delta T_{\text{internal}} = T_{\text{max}} - \bar{T}_{\text{wall}}$, in this case is only 0.56 K and is much less than the average external temperature rise in the biocrystal which was given as $\Delta T_{\text{outside}} = \bar{T}_{\text{wall}} - T_{\text{gas}} = 7.16$ K in Fig. 4(b).

5. Effect of the cooling stream velocity

Increasing the gas stream velocity improves the rate of convective heat transfer from the biocrystal surface to the gas stream. Fig. 7 shows the local variation of h_{θ} over the surface of the sphere for three different values of gas velocity. As the gas velocity increases, the local and average convective heat-transfer coefficients increase. The h_{θ} value at the stagnation point is greater for higher velocities and reduces over the surface of the crystal until the point of flow separation, and is about the same at that point for all three different gas velocities. The increase in local h_{θ} in the back region of the crystal is dependent on the strength of the recirculation velocity, which in turn is dependent on the free-stream velocity. In steady laminar flow, the higher the upstream velocity the larger the recirculation zone and the stronger the recirculation velocities and gradients, and thus the local value of h_{θ} is higher in that region. A review of the relevant fluid mechanics literature shows (Lee, 2000) that the recirculation region remains attached and symmetric about the axis passing through the center of the sphere up to a maximum Reynolds number of $\text{Re} = 220$ ($U_{\infty} \leq 1.90$ m s⁻¹ for 0.2 mm sphere

Table 4

Effect of thermal conductivity k on \bar{h} , $\Delta T_{\text{outside}}$ and $\Delta T_{\text{internal}}$.

The change in k affects only $\Delta T_{\text{internal}}$, which decreases with increasing k . A change in k does not appreciably alter either \bar{h} or $\Delta T_{\text{outside}}$.

k (W m ⁻¹ K ⁻¹)	\bar{h} (W m ⁻² K ⁻¹)	$\bar{T}_{\text{wall}} - T_{\infty}$ (K)	$T_{\text{max}} - \bar{T}_{\text{wall}}$ (K)
0.06	354.2	7.44	4.682
0.6	346.0	7.16	0.556
6	343.6	7.10	0.0593

cooled by N₂ gas), and remains attached but asymmetric for $220 < \text{Re} \leq 350$, while still within the laminar flow regime. For $\text{Re} > 350$, the flow starts shedding with oscillating alternating vortices that eventually becomes unstable and transition to turbulence occurs.

Table 3 shows the variation in the average heat-transfer coefficient, \bar{h} , the external temperature rise, $\Delta T_{\text{outside}} = \bar{T}_{\text{wall}} - T_{\infty}$, and the internal temperature difference, $\Delta T_{\text{internal}} = T_{\text{max}} - \bar{T}_{\text{wall}}$, for four different velocities. \bar{h} increases with increasing velocity (second column) and, as a result, the external temperature rise $\Delta T_{\text{outside}}$ (third column) decreases. The variation in flow velocity does not alter the maximum internal temperature difference and $\Delta T_{\text{internal}}$ is almost the same for all of the stated velocities (last column). Rather, $\Delta T_{\text{internal}}$ depends on the rate of internal heat conduction and, in particular, on the value of the thermal conductivity of the biocrystal, as will be shown in the following section.

6. Effect of k_{sphere}

Table 4 shows the effect of varying the thermal conductivity, k_{sphere} , of the biocrystal and shows that the change in the thermal conductivity of the biocrystal affects only the internal region of the biocrystal, *i.e.* $\Delta T_{\text{internal}}$, whereas $\bar{T}_{\text{wall}} - T_{\infty}$, attributed to convection, essentially remains constant. As k_{sphere} increases, $\Delta T_{\text{internal}}$ decreases roughly by the same order of magnitude (last column). The external temperature rise, $\Delta T_{\text{outside}}$, remains almost the same for the three different k values since all calculations produce a similar \bar{h} , as a result of unchanged flow characteristics (same U_{∞}) and fixed heat-source parameters.

7. Effect of varying beam parameters

Another important objective is to analyze the heat transfer under varying beam conditions, specifically different intensity, attenuation length and beam size. Variable beam intensity, I''_0 , is taken into consideration in the present analysis in Table 5. Detailed calculations show that there is no effect on the average heat-transfer coefficient \bar{h} (fourth column) with the change of beam intensity. However, the outside temperature difference (second column) and the maximum internal temperature difference (third column) change significantly. The increase in beam intensity raises $\Delta T_{\text{outside}}$ and $\Delta T_{\text{internal}}$ by roughly the same order of magnitude (*i.e.* temperature

Table 5

Varying beam intensity.

The intensity of the beam is changed, keeping the beam area constant and its effect on $\Delta T_{\text{outside}}$, $\Delta T_{\text{internal}}$, \bar{h} and q deposited is shown. With increasing intensity, $\Delta T_{\text{outside}}$, $\Delta T_{\text{internal}}$ and q deposited increase, but there is no change in \bar{h} .

I_0'' (photons $\text{mm}^{-2} \text{s}^{-1}$)	$\bar{T}_{\text{wall}} - T_{\infty}$ (K)	$T_{\text{max}} - \bar{T}_{\text{wall}}$ (K)	\bar{h} ($\text{W m}^{-2} \text{K}^{-1}$)	q (W)
4.00×10^{13}	0.589	0.0246	345.9	0.0000254
4.00×10^{14}	7.16	0.556	346.0	0.000308
4.00×10^{15}	72.8	5.60	346.0	0.00313

increase is roughly linear with beam intensity). Table 6 shows how the variation in L_{att} affects temperature. The variation in L_{att} is due to either different incident beam energy or changes in material properties. As L_{att} decreases, q_{absorbed} increases (last column) and therefore there is a corresponding increase in both the external temperature rise, $\Delta T_{\text{outside}}$, and the internal temperature difference, $\Delta T_{\text{internal}}$. Again \bar{h} remains approximately the same owing to the unchanged fluid flow properties and almost isothermal surface wall temperature.

The effect of beam size (Table 7) is investigated relative to the reference case (50%) by either expanding it to full beam diameter ($D_b = D_s$ or 100%) or by focusing it down to 25% or 10% diameter, while keeping the incident power constant. This was achieved by decreasing (or increasing) the incident intensity for the full (or focused) beam as discussed earlier. A relatively small change in the maximum internal temperature difference is observed (column 2) with the change in beam size; the internal temperature difference, $\Delta T_{\text{internal}}$, reduced from 1.3 K for the 10% beam to 0.2 K for the 100% (full) beam but overall the magnitude of the internal temperature difference is still rather small relative to the outside temperature increase. The external temperature rise, $\Delta T_{\text{outside}}$, (third column) reduced from 7.6 K to 5.0 K by changing from the 10% to the 100% beams, respectively. It can be observed that the external temperature difference is almost constant for all of the three focused beams (*i.e.* 10%, 25% and 50% beams) owing to the fact that the power absorbed is almost identical for these three cases (last column), and since \bar{h} (fourth column) remains the same. However, in the case of the 100% (full) beam, there is less power absorbed in comparison with the focused beams, even though the incident power, *i.e.* $A_B I_0''$, is kept fixed in all four calculations. This is due to the large variation in the absorption path length for the source beam over the surface of the spherical biocrystal, *i.e.* absorption depth reduces to zero at both the top and bottom. Less total energy is absorbed and the similar \bar{h} results in a smaller external temperature rise.

Fig. 8 shows plots of the internal temperature distribution inside the biocrystal at the mid-depth from the side (Fig. 8a) and the front (Fig. 8b), changing from focused (10%) to full (100%) incident source beam sizes. The side-view contours for 10% source beam size clearly show higher temperatures in the cylindrical region in which the energy from the source beam is absorbed compared with the rest of the sphere. Also, it can be noted that the hotter region is shifted towards the rear of the

Table 6

Effect of varying absorption length, L_{att} .

The change in L_{att} affects $\Delta T_{\text{outside}}$, $\Delta T_{\text{internal}}$ and q deposited, with \bar{h} remaining practically constant. $\Delta T_{\text{outside}}$, $\Delta T_{\text{internal}}$ and q deposited decrease with increase in absorption length.

L_{att} (mm)	$\bar{T}_{\text{wall}} - T_{\infty}$ (K)	$T_{\text{max}} - \bar{T}_{\text{wall}}$ (K)	\bar{h} ($\text{W m}^{-2} \text{K}^{-1}$)	q (W)
1.9	14.1	1.07	349.9	0.000607
3.9	7.16	0.556	346.0	0.000308
5.2	4.76	0.375	346.1	0.000205

Table 7

Effect of the size of the X-ray beam.

A large change in beam size (maintaining same total flux) results in only modest change in $\Delta T_{\text{internal}}$ and does not affect \bar{h} . The major temperature difference is still $\Delta T_{\text{outside}}$ which depends on \bar{h} and on the total amount of q absorbed.

Beam size	$T_{\text{max}} - \bar{T}_{\text{wall}}$ (K)	$\bar{T}_{\text{wall}} - T_{\infty}$ (K)	\bar{h} ($\text{W m}^{-2} \text{K}^{-1}$)	q (W)
10%	1.30	7.60	345.3	0.000326
25%	0.904	7.65	345.5	0.000329
50%	0.556	7.16	346.0	0.000308
100%	0.216	5.06	347.6	0.000218

biocrystal owing to lower local convective heat-transfer coefficient, h_{θ} , in the wake. For the full-beam case, the isotherms (lines of constant temperature) appear more circular in shape, owing to the fact that energy is almost uniformly deposited over the entire spherical region in the biocrystal. As the beam is focused the temperature contours are more localized near the central core region. However, irrespective of the extent of localization, the energy absorbed is redistributed over the entire spherical region owing to thermal diffusion. The maximum temperature attained in each case decreases as the beam area increases, owing to almost the same amount of energy being distributed over a larger cylindrical beam region and because of closer proximity to the convectively cooled exterior surface. Fig. 8(b) shows the temperature distribution inside the biocrystal at the mid-depth from the front. The isotherms form concentric rings with closer spacing of contours concentrated (i) in the central cylindrical region in which the focused beam energy is absorbed, and also (ii) at the surface in the surrounding thermal boundary layer. The sharper temperature gradients located outside the surface are due to convection heat transfer.

Figs. 9(a) and 9(b) show the axial temperature profiles along the centerline of the biocrystal in the Z (side view, from front to back) and X (front view, from left to right) directions, respectively. From the side profiles (top plot) it can be clearly seen that the maximum centerline temperature, T_{max} , is shifted towards the rear of the biocrystal. This is attributed to the fact that the local heat-transfer coefficient, h_{θ} , is lower in that region. Also, the magnitude of $T_{\text{centerline}}$ is greatest for 10% beam (solid line) and reduces as the beam size increases to 25% and 50% (dashed lines), owing to similar amounts of energy being deposited into a larger region that is closer to the gas stream having lower temperature. Also shown is $T_{\text{centerline}}$

Table 8

Effect of crystal size, keeping all other parameters fixed.

An increase in crystal size increases the q deposited. However, owing to an increase in \bar{h} and a large increase in surface area of the crystal, $\Delta T_{\text{outside}}$ decreases. The change in $\Delta T_{\text{internal}}$ is almost negligible.

D_{sphere} (mm)	Area (m ²)	\bar{h} (W m ⁻² K ⁻¹)	$\bar{T}_{\text{wall}} - T_{\infty}$ (K)	$T_{\text{max}} - \bar{T}_{\text{wall}}$ (K)	q (W)
0.2	1.26×10^{-7}	346.0	7.16	0.556	0.000308
0.4	5.02×10^{-7}	406.7	6.06	0.543	0.000630
0.8	2.01×10^{-6}	458.3	5.88	0.560	0.00121

for the 100% beam (dot-dashed line) case, which is considerably lower than the focused-beam results, owing to the reduced amount of absorbed energy caused by the overall shorter absorption path length at the top and at the bottom of the spherical biocrystal. Fig. 9(b) shows $T_{\text{centerline}}$ profiles in the x direction. This plot again shows that the maximum temperature is highest for the 10% beam but diminishes (and the profile ‘spreads out’) with the increase in beam size. T_{max} peaks at the exact geometric center of the plot because of the symmetry of the fluid flow field and the heat source distribution in the x direction, across the flow stream.

Finally, superimposed in Figs. 9(a) and 9(b) are the temperature profiles calculated for the case of a spherical biocrystal obtained from a simpler one-dimensional thermal model assuming a uniform convective heat-transfer coefficient h (i.e. spatial variation neglected). The amount of energy deposited, q , used in this simpler analytical model is set equal to the same amount that is absorbed in the 100% beam size case having non-uniform h , but is evenly distributed throughout the sphere. Also, the convective heat-transfer coefficient h assumed here is set equal to the average convection heat-transfer coefficient calculated over the entire surface of the biocrystal from our CFD model. This average value is the same value everywhere, thus rendering this thermal model truly one-dimensional and permitting a very easy analytical solution (Kriminski *et al.*, 2003). It can be seen that the temperature profiles generated from this simplified model (bottom solid line in both upper and lower plots) are symmetric in both side and front views (z and x directions, respectively). Also, the values of $T_{\text{centerline}}$ for the one-dimensional case are very similar in magnitude to the more advanced numerical solution for the 100% beam case with non-uniform h_{θ} calculated over the surface of the biocrystal. Thus, the difference between the two sets of lines can be attributed mainly to the variation in local h_{θ} and is not very large if the energy is deposited throughout the sphere (i.e. full beam). However, it is expected that the differences between the results generated by the two different models will become more pronounced as the X-ray beam is increasingly focused.

8. Effect of crystal size

Table 8 and Fig. 10 show the effect of increasing the crystal diameter from 0.2 mm to 0.4 mm to 0.8 mm, keeping the source beam target area, beam intensity and velocity of the N₂ gas stream the same in all three cases. Numerical computa-

Table 9Comparison showing N₂ versus He gas cooling (for same gas jet velocity).

He at 30 K results in three times larger \bar{h} than N₂ at 100 K and therefore a lower $\Delta T_{\text{outside}}$. The higher thermal conductivity of the crystal at lower temperature is responsible for the smaller $\Delta T_{\text{internal}}$ shown.

Gas	\bar{h} (W m ⁻² K ⁻¹)	$\bar{T}_{\text{wall}} - T_{\infty}$ (K)	$T_{\text{max}} - \bar{T}_{\text{wall}}$ (K)
N ₂ @ 100 K	346.0	7.16	0.556
He @ 30 K	1078.4	2.28	0.0560

tions show that the average heat-transfer coefficient, \bar{h} , increases (column 3) from 346 to 458 W m⁻² K⁻¹ with increasing crystal size. Moreover, there is a very large increase ($\sim 16\times$) in the surface area (column 2) of the biocrystal. Both of these factors will enhance the rate of convective heat transfer and lower the crystal temperature. However, coupled with this, the energy deposited in the biocrystal increases with increasing crystal size (last column) owing to the longer absorption path length, which will raise the temperature of the sample. With all of these factors taken into account, the numerical calculations show that, as the crystal size increases, the outside temperature difference, $\Delta T_{\text{outside}}$ (fourth column), actually decreases from about 7.2 to 5.9 K, but the maximum internal temperature difference, $\Delta T_{\text{internal}}$ (fifth column), remains almost constant. Although the amount of energy deposited rises with increasing crystal size, the increase in average convective heat-transfer coefficient, \bar{h} , and greater surface area dominate, resulting in a lower outside temperature difference, $\Delta T_{\text{outside}}$. Fig. 10 shows the internal temperature contours for all three crystal diameters, 0.2, 0.4 and 0.8 mm, when exposed to the same X-ray beam. Clearly the temperature is highest in the cylindrical region in which the energy is deposited. Energy is then conducted away through the rest of the sphere volume to its outer wall, but still the temperature differences inside the largest crystal are relatively small. The rear of the sphere is again hotter compared with the front owing to the relatively lower value of the local convective heat-transfer coefficient, h_{θ} , in the wake region of the biocrystal. A much greater reduction in crystal temperature is possible if the system geometry can be changed such that the surface area is increased without increasing the amount of energy deposited, for example by using larger and flatter (constant thickness) crystals.

9. Effect of gas properties

Another numerical computation was performed by changing the gas coolant from N₂ at 100 K to He at 30 K as well as changing the thermal conductivity of the biocrystal sample from 0.6 to 5 W m⁻¹ K⁻¹. It is expected that the thermal conductivity of the material increases with decreasing temperature, here from 100 K to 30 K (Dillard & Timmerhaus, 1966; Klemens, 1969; Kaviany, 2002). The various thermo-physical properties for both N₂ and He gases at 100 K and 30 K, respectively, are listed in Table 1. Table 9 shows the difference in average heat-transfer coefficient \bar{h} , $\Delta T_{\text{outside}}$ and

radiation damage

$\Delta T_{\text{internal}}$ (second, third and fourth columns, respectively) owing to changing the gas coolant from N_2 to He. The numerical simulations reveal that \bar{h} for He gas is approximately three times higher than that of the N_2 gas (1078 versus $346 \text{ W m}^{-2} \text{ K}^{-1}$). This results in a proportionally sharp reduction in external temperature difference of $\Delta T_{\text{outside}} = 7.2 \text{ K}$ for a biocrystal with N_2 at 100 K to $\Delta T_{\text{outside}} = 2.3 \text{ K}$ when using He at 30 K. Also, the internal temperature difference, $\Delta T_{\text{internal}}$, is much lower compared with the N_2 gas case, not owing to the enhanced rate of convection but rather because of the higher thermal conductivity of the material sample used in the conduction analysis. As presented earlier, $\Delta T_{\text{internal}}$ is inversely proportional to the thermal conductivity of the material and hence an increase in thermal conductivity of the material decreases $\Delta T_{\text{internal}}$ by approximately the same

order. The flow field surrounding the biocrystal calculated from the numerical analysis when cooled with He gas is shown in Fig. 11. It appears very similar in shape to the flow pattern described in Fig. 4(a) for N_2 gas cooling, except that the size of the recirculation zone located behind the sphere is much shorter in length. Likewise, comparison of the local convection

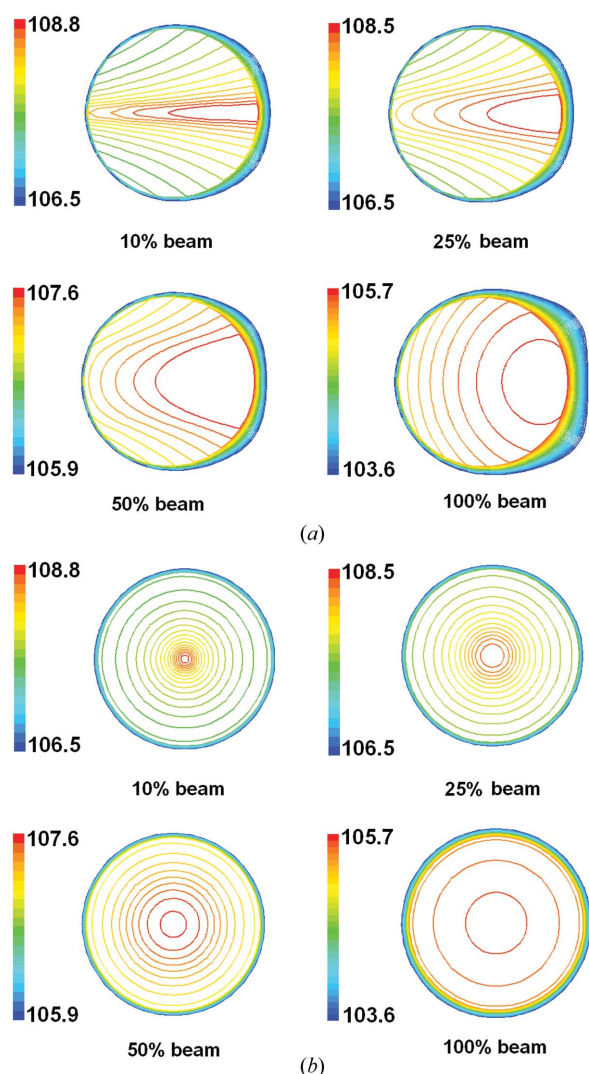


Figure 8 Isotherms (constant temperature contours in K) inside the biocrystal for four different sizes of X-ray beam with constant flux, showing the internal temperature distribution dependence on the size of the source beam (*i.e.* on the flux density). Smaller more focused X-ray beams result in sharper internal temperature gradients (energy is deposited in a smaller region) and slightly higher maximum temperatures, although the average bulk temperature of the sphere remains fairly constant: (a) side view (YZ plane) and (b) front view (XY plane).

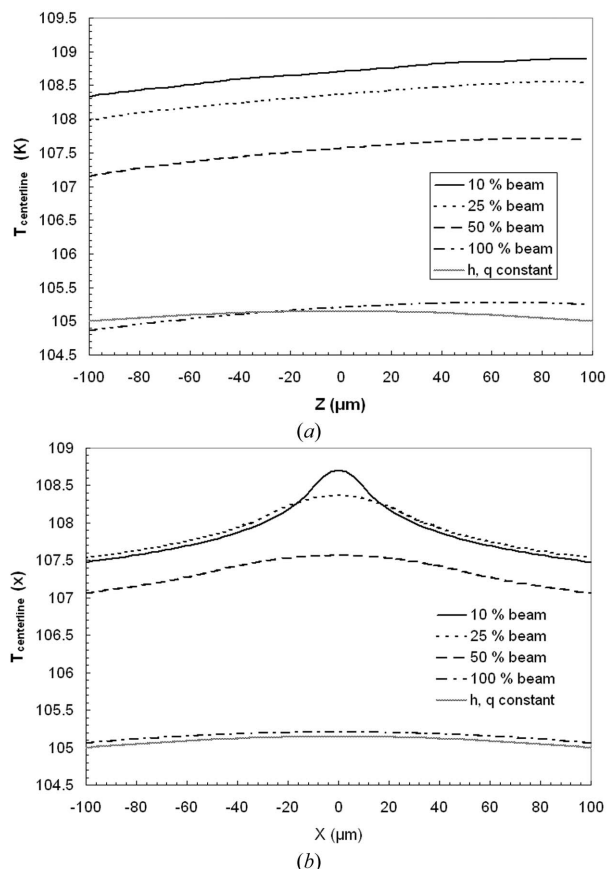


Figure 9 Temperature profiles calculated for the different beam sizes (along with analytical one-dimensional solution assuming uniform h): (a) side view; (b) front view. The sphere temperature increases as the X-ray beam is focused. Along the flow stream direction (z -direction profiles) the temperatures are higher at the rear of the sphere, and are highest at the center of the sphere (and symmetrical) when traversing normal to the flow stream direction (x -direction profiles).

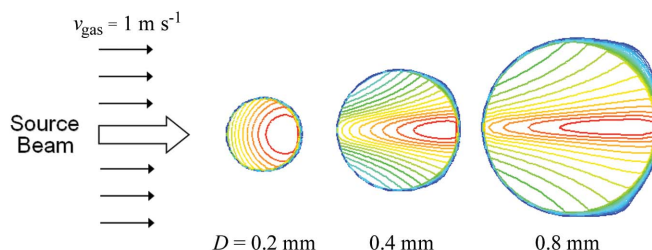


Figure 10 Internal temperature distribution for different-sized crystals exposed to the same (reference) beam. The target area irradiated by the source beam is held fixed but more energy is deposited for thicker crystals. However, the maximum internal temperature difference remains almost the same in all cases and the outside temperature difference decreases owing to the added surface area for convection. Refer to Table 8 for the actual temperature differences.

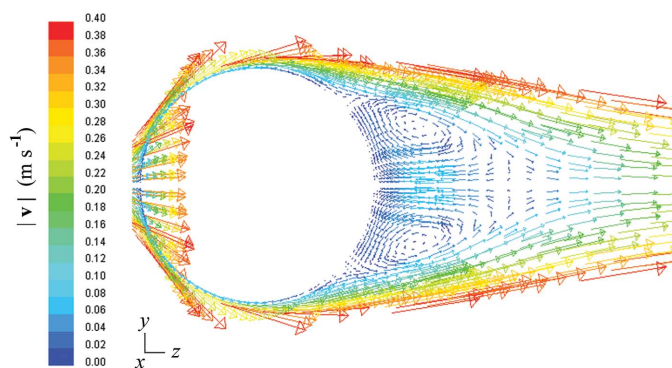


Figure 11
Velocity field for He gas stream flowing past the sphere depicted by velocity vectors. The flow pattern is similar to that obtained using N₂ gas except that the recirculation zone is slightly shorter.

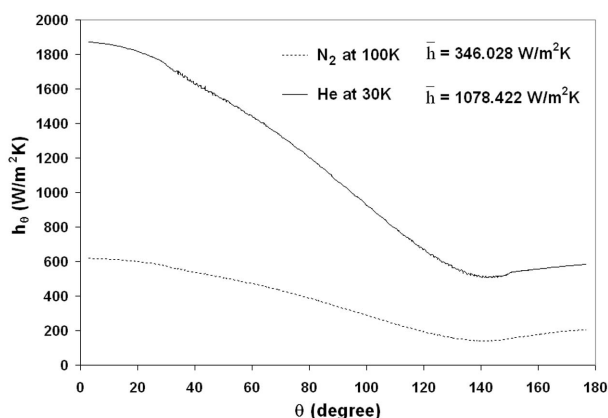


Figure 12
Local h_θ variation along the surface of the sphere for He gas cooling at 30 K plotted with N₂ at 100 K for the same gas stream velocity, showing significant increase in h_θ at all locations. Comparison shows that He gas outperforms N₂ gas in terms of higher local h_θ and average \bar{h} heat-transfer coefficients.

coefficients for the two different gases (Fig. 12) reveals very similar behavior in terms of spatial dependence, but shows the large difference in the magnitudes, essentially owing to the differing values of thermal conductivity of the two gases (*i.e.* difference in gas properties and not flow patterns).

10. Conclusions

The temperature increase during intense X-ray beam heating of spherical biocrystals has been carefully analyzed using advanced CFD modeling. Numerical solutions provided the following:

- (i) accurate local h_θ and \bar{h} values for convection;
- (ii) fluid flow and temperature fields surrounding the body;
- (iii) coupled internal temperature distributions within the crystal.

For a typical 0.2 mm-diameter biocrystal, subjected to an intense third-generation 13 keV X-ray beam of 3.14×10^{12} photons s⁻¹ focused on half of the crystal, results show that $\Delta T_{\text{external}} = 7.16$ K and $\Delta T_{\text{internal}} = 0.56$ K. The local heat-

Table 10

Summary of results from the parametric investigation.

The external and internal crystal temperature differences are reported over a range of conditions. The parameters are listed in rank order, the total beam flux being the most important parameter and the beam size (flux density, assuming constant flux) the least, with regard to their impact on crystal temperatures. The convection parameters and crystal size alter the external temperature difference (dominate temperature increase) whereas the internal temperature rise is always minor by comparison.

Parameter	$\Delta T_{\text{external}}$	$\Delta T_{\text{internal}}$
q_{abs} (flux, L_{att})	(~ Linear)	(~ Linear)
k_{sphere}	No effect	(~ Linear)
Gas type (N ₂ → He)	(7 → 2 K)	(0.5 → 0.05 K)
Gas velocity (0.5 → 2 m s ⁻¹)	(9 → 6 K)	Negligible
Crystal size (0.2 → 0.8 mm)	(7 → 6 K)	Negligible
Beam size (100 → 10%)	Negligible	(0.2 → 1.3 K)

transfer coefficient, h_θ , varied from 614 to 130 W m⁻² K⁻¹ over the surface of the sphere and the average heat-transfer coefficient was $\bar{h} = 346$ W m⁻² K⁻¹. Using the numerical model, the investigation presented the effect of several parameters, such as the gas stream velocity U_∞ , thermal conductivity of the sphere k_{sphere} , three beam parameters (beam intensity I_0'' , absorption length L_{abs} and beam size D_b), crystal size and the type of gas coolant, to obtain the expected temperature rise over a range of different operating conditions. The comparison of results, in order of greatest to least importance, with respect to both external and internal temperature difference is shown in Table 10. Total thermal load, convection rate and crystal size were the main controlling factors that determined the sample temperature. Beam size had less impact since internal heat conduction resulted in effective thermal spreading of the deposited energy.

It was shown that, in general, the internal temperature rise within small crystals is relatively small, *i.e.* $\Delta T_{\text{internal}} \simeq 0.5$ K, and is about the same order of magnitude for both full and focused beams owing to the efficient thermal spreading by internal thermal diffusion, *i.e.* heat conduction. The major temperature increase is in the external temperature rise, $\Delta T_{\text{outside}} = \bar{T}_{\text{wall}} - T_\infty$, which is about 7 K and is limited by the rate of convective heat transfer. It was shown that using bigger spherical crystals (for fixed beam size) results in lower temperatures than for smaller crystals owing to the added surface area for convection (but much greater improvement is expected if the surface area for convection is increased without increasing the absorption depth). Finally, a brief comparison of the more sophisticated three-dimensional CFD results against the simpler one-dimensional model (uniform h) solution showed that the actual spatial variation in the convective heat-transfer coefficient (caused by the surrounding fluid flow field) results in slightly elevated temperatures in the back region of the biocrystal. However, this has only a rather minimal effect on the bulk crystal temperatures owing to the relatively small crystal size and efficient thermal spreading by internal heat conduction. Hence it is concluded that, in terms of simplified thermal modeling of small crystals, one may reasonably calculate an approximate $\Delta T_{\text{outside}}$ using an average \bar{h} that is obtained from an accurate

empirical convection correlation, and estimate maximum $\Delta T_{\text{internal}}$ using a simple one-dimensional heat conduction solution.

11. Recommendations for future work

The shape of the biocrystal surrounded by mother liquor was considered to be a sphere, which at best is only a rough approximation; more realistic geometry should be modeled to accurately simulate fluid flow and convective heat transfer from actual crystal/loop systems. The thermophysical properties used in the present study are based on values from the prior literature, which are estimates based on available resources and need to be more accurately determined. The thermal conductivity of the mother liquor and the crystal were taken to be the same; however, differences between cryoprotectant mixtures and crystal properties should be taken into account as well as perhaps local impurities and possible non-homogeneities in the crystal itself. Transient temperature behavior is an important aspect of the problem that needs to be studied, especially the time required to achieve steady-state conditions under continuous beam compared with pulsed-beam operations. The last, and perhaps the most important, recommendation at this time is to experimentally verify these temperature predictions in a series of carefully controlled experiments at a participating synchrotron.

References

- Dillard, D. S. & Timmerhaus, K. D. (1966). *Pure Appl. Cryogen.* **4**, 35–44.
- Garman, E. (1999). *Acta Cryst.* **D55**, 1641–1653.
- Garman, E. & Schneider, T. R. (1997). *J. Appl. Cryst.* **30**, 211–237.
- Helliwell, J. R. (1992). *Macromolecular Crystallography with Synchrotron Radiation*, pp. 260–268. Cambridge University Press.
- Hope, H. (1990). *Annu. Rev. Biophys. Biophys. Chem.* **19**, 107–126.
- Kaviany, M. (2002). *Principles of Heat Transfer*, pp. 183–195. New York: Wiley.
- Kazmierczak, M. J. (2001). *Second International Workshop on X-ray Damage to Crystalline Biological Samples*, Argonne National Laboratory, Argonne, Illinois, USA. Abstract.
- Klemens, P. G. (1969). *Thermal Conductivity*, Vol. 1, edited by R. P. Tye, pp. 2–68. London: Academic Press.
- Kriminski, S., Kazmierczak, M. J. & Thorne, R. A. (2003). *Acta Cryst.* **D59**, 697–708.
- Kuzay, T. M., Kazmierczak, M. J. & Hsieh, B. J. (2001). *Acta Cryst.* **D57**, 69–81.
- Lee, S. (2000). *Comput. Fluids*, **29**, 639–667.
- Mhaisekar, A., Kazmierczak, M. J. & Banerjee, R. (2005). *Num. Heat Trans. J. Part A*. In the press.
- Nicholson, J., Nave, C., Fayz, K., Fell, B. & Garman, E. (2001). *Nucl. Instrum. Methods Phys. Res. A*, **467/468**, 1380–1383.
- Rodgers, D. W. (1994). *Structure*, **2**, 1135–1140.
- Rosenbaum, G. & Kazmierczak, M. J. (2002). *Acta Cryst.* **A58**(Suppl.), C279.
- Weik, M., Ravelli, R. B. G., Kryger, G., McSweeney, S., Raves, M. L., Harel, M., Gros, P., Silman, I., Kroon, J. & Sussman, J. L. (2000). *Proc. Natl. Acad. Sci. USA*, **97**, 623–628.
- Whitaker, S. (1972). *AIChE J.* **18**, 361–371.